



AFRL-AFOSR-JP-TR-2022-0004

Programming of Graphene Properties via Defect Design and Characterization

Park, Won
HANYANG INDUSTRY-UNIVERSITY COOPERATION
HAENGDANG 1DONG, SEONGDONG-GU, SEOULRM110. HIT, HANYANG UNIV. 17
SEOUL, ,
KR

11/22/2021
Final Technical Report

DISTRIBUTION A: Distribution approved for public release.

Air Force Research Laboratory
Air Force Office of Scientific Research
Asian Office of Aerospace Research and Development
Unit 45002, APO AP 96338-5002

REPORT DOCUMENTATION PAGE

Form Approved
OMB No. 0704-0188

The public reporting burden for this collection of information is estimated to average 1 hour per response, including the time for reviewing instructions, searching existing data sources, gathering and maintaining the data needed, and completing and reviewing the collection of information. Send comments regarding this burden estimate or any other aspect of this collection of information, including suggestions for reducing the burden, to Department of Defense, Washington Headquarters Services, Directorate for Information Operations and Reports (0704-0188), 1215 Jefferson Davis Highway, Suite 1204, Arlington, VA 22202-4302. Respondents should be aware that notwithstanding any other provision of law, no person shall be subject to any penalty for failing to comply with a collection of information if it does not display a currently valid OMB control number.
PLEASE DO NOT RETURN YOUR FORM TO THE ABOVE ADDRESS.

1. REPORT DATE (DD-MM-YYYY) 22-11-2021	2. REPORT TYPE Final	3. DATES COVERED (From - To) 26 Jul 2018 - 25 Jul 2021
--	--------------------------------	--

4. TITLE AND SUBTITLE Programming of Graphene Properties via Defect Design and Characterization	5a. CONTRACT NUMBER FA2386-18-1-4110
	5b. GRANT NUMBER
	5c. PROGRAM ELEMENT NUMBER

6. AUTHOR(S) Won Park	5d. PROJECT NUMBER
	5e. TASK NUMBER
	5f. WORK UNIT NUMBER

7. PERFORMING ORGANIZATION NAME(S) AND ADDRESS(ES) HANYANG INDUSTRY-UNIVERSITY COOPERATION HAENGDANG 1DONG, SEONGDONG-GU, SEOULRM110. HIT, HANYANG UNIV. 17 SEOUL, KR	8. PERFORMING ORGANIZATION REPORT NUMBER
--	---

9. SPONSORING/MONITORING AGENCY NAME(S) AND ADDRESS(ES) AOARD UNIT 45002 APO AP 96338-5002	10. SPONSOR/MONITOR'S ACRONYM(S) AFRL/AFOSR IOA
	11. SPONSOR/MONITOR'S REPORT NUMBER(S) AFRL-AFOSR-JP-TR-2022-0004

12. DISTRIBUTION/AVAILABILITY STATEMENT
A Distribution Unlimited: PB Public Release

13. SUPPLEMENTARY NOTES

14. ABSTRACT
Defects play an important role in crystalline materials, making the actual properties quite different from defect-free perfect crystals. For example, in semiconductors, an extremely small amount of impurity dopants can significantly change the electrical properties so that Si can have either p-type or n-type characteristics. Especially in graphene and other 2-dimensional (2D) materials, most defects are exposed to the outside and thus, they are supposed to have a more critical effect on the properties. Here, we propose programming graphene properties via defect design and functionalization on the basis of high-quality nano-patterned graphene with disordering yet with contamination-free edges and a near-single crystal structure. Most chemical vapor deposition (CVD) grown graphene has many defects, such as grain boundaries (GBs), point defects, and wrinkles. These defects are developed randomly, and thus they are difficult to control. So, to engineer the defects and to program the properties, we first established the growth of high-quality, single-crystal graphene to minimize the unintentionally incorporated defects such as GBs. We then carried out engineering edge defects in graphene by introducing artificial defects in graphene or growing edge-controlled flakes and characterized these defects depending on the edge chirality. Although conventional graphene patterning via lithography and etching has been suggested to introduce edge defects in graphene, this approach causes C atoms at the edges to become disordered and contaminated with residues and thus lose the intrinsic properties of the defects. Here, we suggested defect design and functionalization by developing contamination-free edge defects and wrinkles. Further, we expand our scope to 2D semiconducting materials, transition metal dichalcogenides (TMDCs). Unlike semi-metal graphene or insulator h-BN, these TMDC materials have semiconducting properties, with various bandgaps, Indirect to Direct bandgap transition for monolayer cases, and the capability to construct van der Waals heterostructures, as suitable for optoelectronic devices and quantum emitter as well. The uniqueness of our proposed research in addressing this challenge is in the • innovation of the growth technique for engineering defects in graphene with minimal unintentional/intrinsic defects; • substantial experimental and theoretical collaboration for understating the fundamentals at the atomic-scale, thus elucidating correlations between defects and graphene properties; • programming of predictable and improved performance with specific defect design and functionalization strategies. • fabrication and characterization of van der Waals heterostructures of 2D materials with defects design for novel applications Through this project, we resolve the fundamental barrier of the existing technique for engineering graphene defects by achieving a substantial decrease in contamination/disordering due to edge defects, which provides the basis/opportunities for • understanding the intrinsic characteristics of defects in graphene and 2D semiconductor materials • exploiting the engineered defects to control the properties and/or improve the performance of graphene-based electronic/optoelectronic devices for Air Force relevant applications in electronics, photonics, and sensing.

15. SUBJECT TERMS

16. SECURITY CLASSIFICATION OF:			17. LIMITATION OF ABSTRACT	18. NUMBER OF PAGES	19a. NAME OF RESPONSIBLE PERSON
a. REPORT	b. ABSTRACT	c. THIS PAGE			TONY KIM
U	U	U	SAR	20	19b. TELEPHONE NUMBER (Include area code) 315-227-7008

Standard Form 298 (Rev.8/98)
Prescribed by ANSI Std. Z39.18

Section 2: Technical Report PDF Upload

Accomplishments

Introduction

Defects play an important role in crystalline materials, making the actual properties quite different from defect-free perfect crystals. For example, in semiconductors, an extremely small amount of impurity dopants can significantly change the electrical properties so that Si can have the either p-type or n-type characteristics. Especially in graphene and other 2-dimensional (2D) materials, most defects are exposed to the outside and thus, they are supposed to have a more critical effect on the properties. Here, we propose programming graphene properties via defect design and functionalization on the basis of high-quality nano-patterned graphene with disordering yet with contamination-free edges and a near-single crystal structure.

Most chemical vapor deposition (CVD) grown graphene has many defects, such as grain boundaries (GBs), point defects, and wrinkles. These defects are developed randomly, and thus they are difficult to control. So, to engineer the defects and to program the properties, we first established the growth of high-quality, single-crystal graphene to minimize the unintentionally incorporated defects such as GBs. We then carried out engineering edge defects in graphene by introducing artificial defects in graphene or growing edge-controlled flakes and characterized these defects depending on the edge chirality. Although conventional graphene patterning via lithography and etching has been suggested to introduce edge defects in graphene, this approach causes C atoms at the edges to become disordered and contaminated with residues and thus lose the intrinsic properties of the defects. Here, we suggested defect design and functionalization by developing contamination-free edge defects and wrinkles. Further, we expand our scope to 2D semiconducting materials, transition metal dichalcogenides (TMDCs). Unlike semi-metal graphene or insulator h-BN, these TMDC materials have semiconducting properties, with various band gaps, Indirect to Direct band gap transition for monolayer cases, and the capability to construct van der Waals heterostructures, as suitable for optoelectronic devices and quantum emitter as well. The uniqueness of our proposed research in addressing this challenge is in the

- innovation of the growth technique for engineering defects in graphene with minimal unintentional/intrinsic defects;
- substantial experimental and theoretical collaboration for understating the fundamentals at the atomic-scale, thus elucidating correlations between defects and graphene properties;
- programming of predictable and improved performance with specific defect design and functionalization strategies.
- fabrication and characterization of van der Waals heterostructures of 2D materials with defects design for novel applications

Through this project, we resolve the fundamental barrier of the existing technique for engineering graphene defects by achieving a substantial decrease in contamination/disordering due to edge defects, which provides the basis/opportunities for

- understanding the intrinsic characteristics of defects in graphene and 2D semiconductor materials
- exploiting the engineered defects to control the properties and/or improve the performance of graphene-based electronic/optoelectronic devices for Air Force relevant applications in electronics, photonics, and sensing.

Statement of Objectives

- Synthesis of single crystal-like nano-patterned graphene with an artificially-regulated topology, size and spacing of a hole array.
- Characterization of defects in nano-patterned graphene by a combined theoretical-experimental investigation.
- Programming of nano-patterned graphene properties by control of atomic and molecular interactions.
- Fabrication and characterization of 2D van der Waals heterostructures based on defects

Accomplishments during this reporting period

Technical developments.

I. Large-scale single crystal graphene growth on Cu foils

We have developed single-crystal Cu foils with (100) or (111) crystal directions. Commercial 25 mm thick polycrystalline Cu foil was annealed at 1030°C or 1,050°C to obtain Cu (100) or Cu (111), respectively, with H₂ gas flow of 280 sccm. After 60 minutes, the Cu foil was quickly cooled to room temperature. The polycrystalline Cu foils were converted into a nearly single-crystal foil with a specific atomic composition over a wide area depending on the annealing temperature.

In addition, single-crystal graphene was developed using a CVD method using a NaCl additive. The Cu foil was placed in a quartz tubular reactor with a ceramic bottle containing about 3 g of NaCl. A single crystal Cu(111) foil was annealed at 1000°C in an H₂ gas flow of 280 sccm for 60 minutes, and then 2 sccm of methane gas was introduced as a precursor to start graphene growth. During growth, the reactor temperature and pressure were maintained at 1000°C and 550 mtorr, respectively. After 10 minutes of graphene growth, the tube was quickly cooled to room temperature.

II. Engineering edge-defects in 2D materials (zigzag vs armchair)

We have developed sharp and clean edge defects of artificially designed high-quality graphene using conventional cheap metal foils. In addition, a new method utilizing NaCl additive on graphene growth allows graphene flakes (GFs) to have a hexagonal shape with well-defined edges. More specifically, GFs are rectangular or hexagonal when grown with NaCl on the surface of Cu (100) or Cu (111), respectively. Importantly, we found that hexagonal flakes with zigzag edges grow on the surface of Cu (111), while rectangular graphene flakes with two types of edges (i.e., zigzag and armchair edges) grow on the surface of Cu (100).

III. Wrinkling of Polymer film in a desired location and direction

We found a graphene-based thin film wrinkle mechanism. This was achieved by (i) patterning the hole arrangement, (ii) hardening the thin polymer film, and (iii) adjusting the out-of-plane deformation of the film. The film was then exposed to O₂ plasma to harden a surface layer of several tens of nanometers thick in photo-resistance films (Fig. 1, III, dark brown). The edge of the photo-resistant film was exposed to O₂ plasma again until the entire layer was cured (Fig. 1, IV), and the thin polymer film was fixed. After the curing process, the organic solvent was etched and rinsed with acetone and methanol (Fig. 1, V) to remove the lower layer of the uncured (soft) photoresist film. When the sample was removed from the methanol solution, the polymer film floated on an organic solvent occupying the space between the film and the substrate. As a result, the trapped solvent gradually evaporated through the hole in the film. As a result, buckling of the thin film occurred, resulting in straight wrinkles interconnected with adjacent holes (Fig. 1, VI).

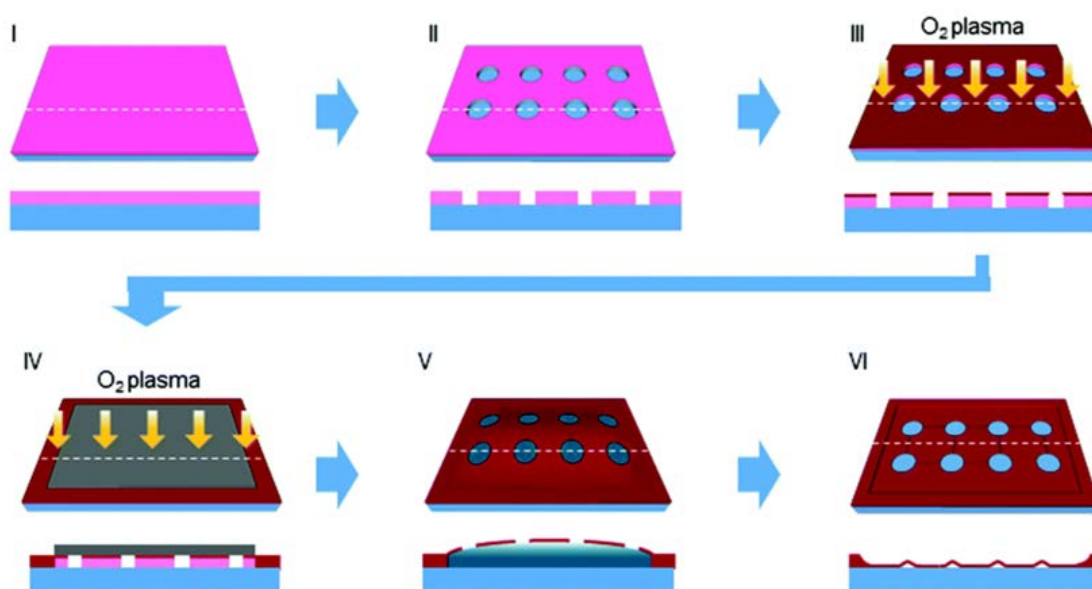


Figure 1. Hardening and wrinkling of a thin polymer film. Schematics of the overall process: patterning of the hole array (I and II), hardening (III and IV), and wrinkling (V and VI). Bottom panels: cross-sectional structures along the dashed lines in the top panel. Note that position of the dashed line in (VI) is different from those in (I-V).

IV. Wrinkling of graphene in a desired location and direction

We have developed a new strategy to create wrinkles in a desired location and direction while suppressing wrinkle formation on unwanted regions, inspired by the spreading and wrinkling phenomena frequently found during wallpapering and/or ironing. To enable this, we introduced a regular array of holes in a graphene-based thin membrane, through which trapping and evaporation of solution between graphene and substrate surface were naturally regulated. This approach generated lattice patterns of graphene/Cu ripples and subsequently graphene wrinkles.

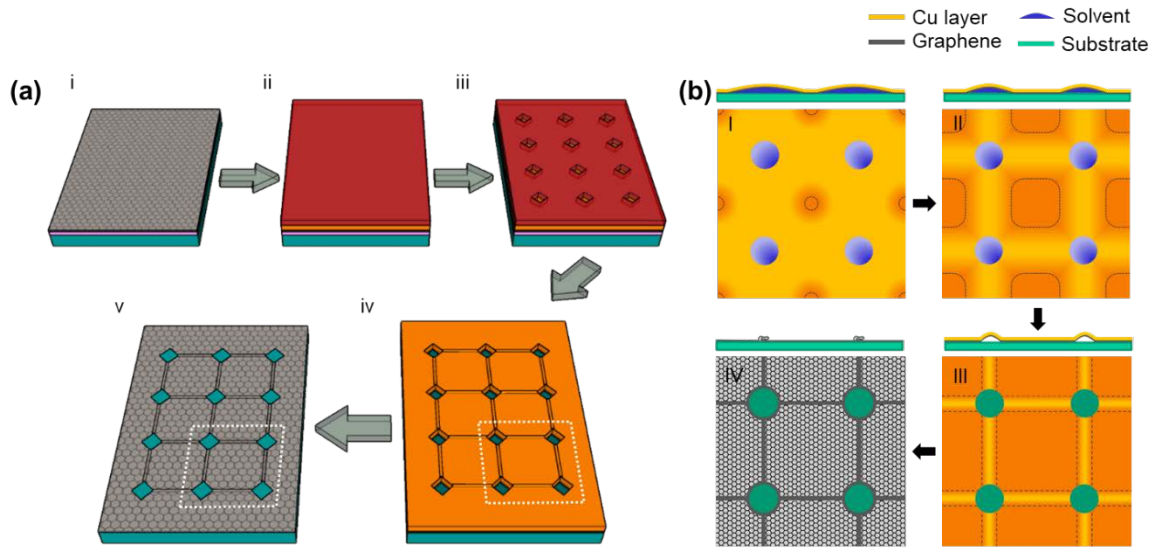


Figure 2. Schematic illustration of graphene/Cu ripple and graphene wrinkle formation. (a) Schematic of the fabrication process of a graphene/Cu ripple (i–iv) and graphene wrinkle (iv–v). (b) Schematic cross-sectional and top views of graphene/Cu rippling (I–III) and graphene wrinkling (III–IV) processes, corresponding to the dashed square region in (a).

V. Selective & epitaxial growth of TMDC networks on graphene wrinkles

We have fabricated a bubbler-type meta-organic chemical vapor deposition (MOCVD) system and synthesized a uniform monolayer MoS₂ and WS₂ film with a size of 1cm X 1cm. Using the bubbler type MOCVD, we can finely control the amount of the source participating in the reaction by precisely adjusting the Ar carrier gas flowing into the bubbler during synthesis. We can synthesize uniform 1-layer TMDCs by inducing layer-by-layer growth in the TMDC growth process by optimizing growth conditions such as precursor, atmosphere gas, H₂ gas flow rate, growth temperature, and growth pressure.

We have demonstrated the epitaxial growth of TMDCs by synthesizing MoS₂ using general poly-crystal graphene and CVD-grown single-crystal graphene developed by our team in the previous study as a template. In addition, we experimentally and computationally analyzed the phenomenon of selective growth of MoS₂ along with the wrinkles (defects) of graphene, suggesting the possibility of forming a 1D network of TMDCs.

VI. Multidimensional atomically-thin TMDC layers on diatom frustules

We developed MOCVD growth of conformal TMDC monolayers and heterostructures on the 3D exoskeletons of diatom frustules. In particular, we showed conformal growth of primarily monolayer TMDCs not only on the outer surface but also inside the pore structure, as confirmed by structural analysis. Characterization and imaging using photoluminescence and micro-Raman analysis revealed that the resulting structures exhibit high-quality, uniform monolayer MoS₂ films in diatom frustums throughout complex morphologies.

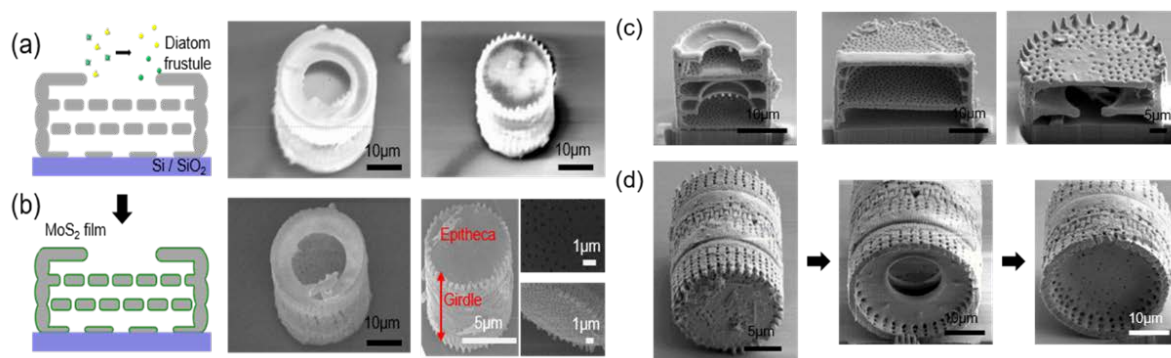


Figure 3. Morphology analysis of MoS₂ diatom frustules. Schematic and SEM images of the diatom frustules before (a) and after (b) the MOCVD growth of MoS₂. (c) Cross-sectional SEM images of the interior of diatom frustules via focused ion beam etching and imaging. (d) Series of cross-sectional SEM images of the diatom *Coscinodiscus centralis* following in-situ etching, which revealed girdles (left image), a valve with a large central hole (center image), and many small holes (right image).

VII. MoS₂ flakes on graphene defects as a membrane for Li-ion filtering

We have fabricated a membrane by selective growth of MoS₂ flakes on multilayer graphene defects (MFs-on-MLGDs) for Li-ion filtering. Figure 4 describes the resulting membrane possesses asymmetric ionic channels consisting of (i) van der Waals interlayer gap between MoS₂ and graphene and (ii) inborn graphene defect. Interestingly, the van der Waals interlayer gap coincides with the optimal size for the Li-ion filtering (~ 0.32 nm) and remains the same at the interface. In addition, the graphene defect with a negatively charged surface provides a more extensive sized inlet for positive ions as analogous to funnel.

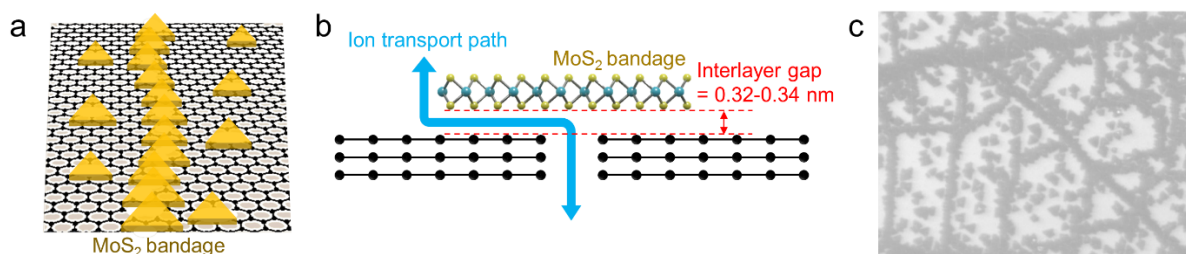


Figure 4. The structure of MFs-on-MLGDs membrane. (a) Schematic illustrating the membrane structures of MFs-on-MLGDs membrane. (b) Cross-sectioned images of the MFs-on-MLGDs membrane describing the ionic transport path. (c) SEM images of the MFs-on-MLGDs membrane.

Using the MFs-on-MLGDs membrane, we have further demonstrated the scaling-up and energy-efficiency strategies. Figure 5 shows the homemade system established by our strategy. 0.1 M HCl and 0.1 M Li/Na/K/Ni/Co chloride solutions are located at the spaces separated by a Nalgene bottle. At the bottle cap of the Nalgene bottle, we pierced a hole then placed the MB-on-GD membrane transferred on the anodic aluminum oxide (AAO) supporting substrate. The polydimethylsiloxane (PDMS) is employed to seal the corner of the membrane (Figure 5a and 5b). The membrane window with 5 mm \times 5 mm for ionic transport is established with PDMS well (the inlet in Figure 5c). The SEM cross-section image shows that the MB-on-GD membrane is successfully transferred on the AAO substrate (Figure 5c).

The operation of the system initiates when the external bias is induced. At the early stage of operation, the external bias only drives the cation transport. Meanwhile, the transport of Li-ion induces the thermodynamically/electrically non-equilibrium state, given that the excess of cations in acidic solution while the shortage of cations in seawater, respectively. At this stage, we increase external bias over 1.23 V and induce the water-splitting reaction, hereby consuming H⁺ ions at the acidic solution ($2\text{H}^+ + 2\text{e}^- \rightarrow \text{H}_2$, 0 V vs. SHE) and supplying H⁺ ions to seawater ($\text{H}_2\text{O} \rightarrow 1/2\text{O}_2 + 2\text{H}^+ + 2\text{e}^-$, 1.23 V vs. SHE). This process adjusts the electric charge neutrality and obtains Li resource in the form of LiCl, a chemically convertible compound. Most importantly, this system enables the electric energies to be multi-functional because they drive the Li-ion transport and generate H₂ gas, which is one of the high-value products for clean energies at the same time.

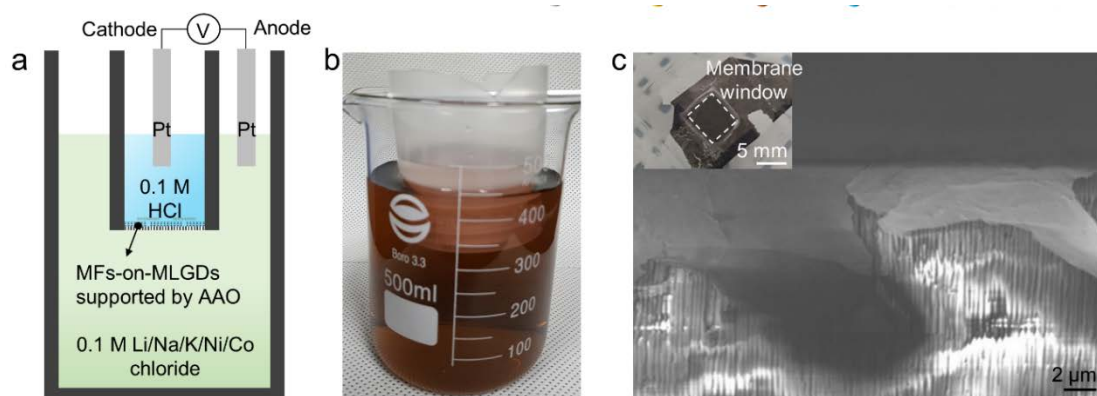


Figure 5. The scaling-up and energy-efficiency strategy using MFs-on-MLGDs membrane. (a) Schematic illustrating the homemade system. The MFs-on-MLGDs membrane separates the acidic solution and mixed solution. (b) Photograph of the homemade system. (c) SEM images showing the MFs-on-MLGDs membrane supported by AAO substrate. The inset is the photograph of MFs-on-MLGDs membrane fixed with the PDMS well.

Result & Discussion: Description of significant experimental advances and their significance.

I. Large-scale single-crystal graphene growth on Cu foils

The polycrystalline Cu foils were converted into single-crystal foils having (100) or (111) orientation according to the high-temperature annealing processes. Structural analysis using electron backscattering diffraction (EBSD) and X-ray diffraction (XRD) shows significant changes in the Cu foil after high-temperature annealing. Previous studies have shown that Cu (100) surface is more stable than that of Cu (111), and thus more energy is needed for the transition from Cu (100) to Cu (111), which is consistent with our results.

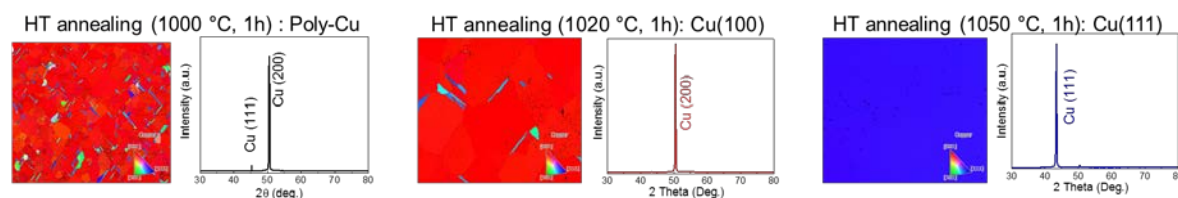


Figure 6. EBSD images and XRD curves for Cu foils with high temperature annealing at (a) 1000°C (b) 1020°C and (c) 1050°C for 1 hour.

Density-functional theory (DFT) free energy calculations demonstrate that NaCl adsorption onto a grain boundary in a monolayer graphene flake causes a reduction of the activation energy. In addition, we find that a few $[\text{Na}^+]$ atoms can cause desorption of oxygen from the surface by examining the effect of a NaCl additive on a Cu(111) model surface with pre-adsorbed oxygen (Figure. 7, 8). Given that the oxygen on Cu surface passivates the nucleation sites, our DFT results support that the oxygen-free surface provides nucleation sites and enhances nucleation events.

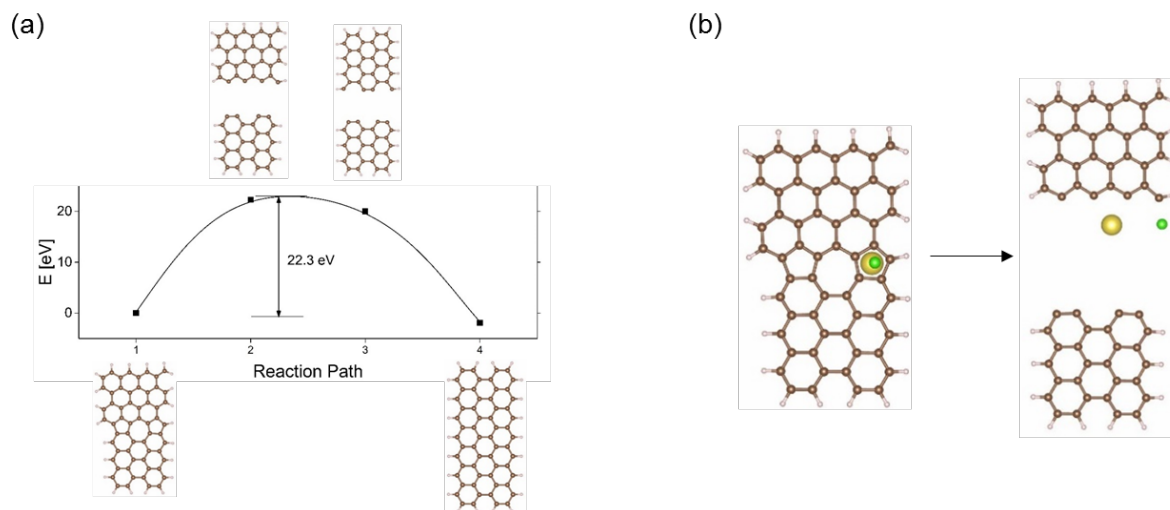


Figure 7. DFT activation energy of healing a grain boundary in monolayer graphene without (a) and with (b) NaCl adsorption, with values of 22.3 eV and 16.1 eV, respectively.

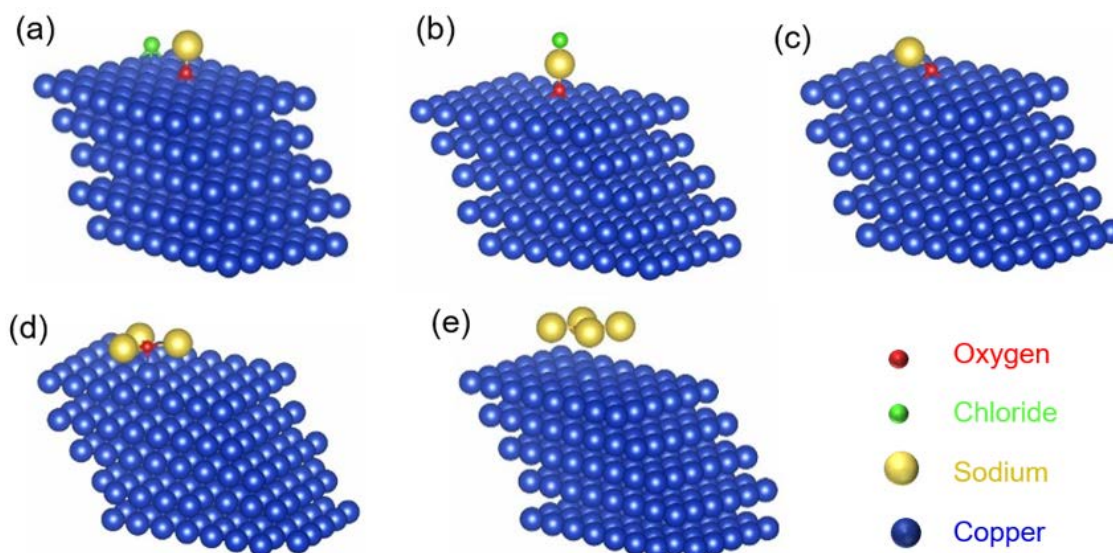


Figure 8. Effects of NaCl adsorption on a Cu(111) surface by DFT calculations. (a,b) NaCl adsorption on a Cu(111) surface with an adsorbed O atom. (c-e). $[\text{Na}^+]$ is shown to assist in desorbing the oxygen atom adsorbed on the Cu(111) surface.

To investigate the role of alkali metal chloride additives in controlling graphene growth, Figure 9 shows the SEM images of early-stage graphene flake growth. Despite the same CVD conditions, GF grown without a NaCl additive results in dendritic morphology, whereas the

addition of NaCl suppresses dendritic growth and leads to polygonal GFs with well-defined edges. In particular, GF is rectangular or hexagonal when grown with NaCl on the surface of Cu (100) or Cu (111), respectively. We have also confirmed that the addition of NaCl significantly increases the nucleation density despite the reduction in the size of individual grains.

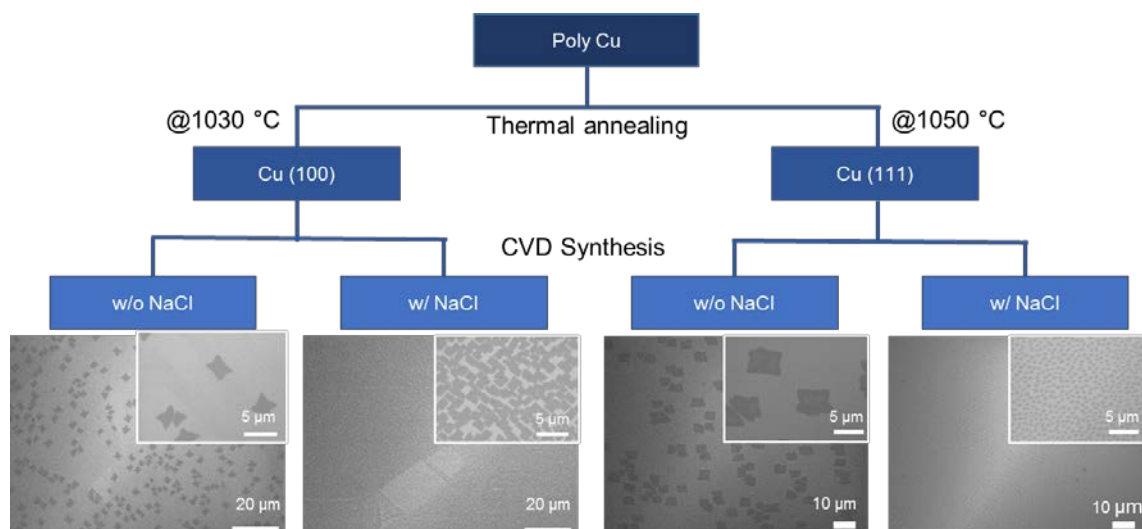


Figure 9. SEM images of graphene flakes on Cu(100) and Cu(111) without and with NaCl additive

To further verify that the epitaxial and seamless stitching of the hGFs on Cu (111) produces single-crystal graphene on a large scale, we utilized transmission electron microscopy (TEM) and selected area electron diffraction (SAED). These results show that graphene has the same crystallographic orientation over a large area. The crystallinity of the graphene was further investigated by the dark-field TEM (DF-TEM). The DF-TEM image, recorded with the diffraction spot marked by circle point of the SAED pattern in Figure. 10b, exhibits uniform brightness over the entire area (Figure. 10e and f), which is further evidence that the crystallographic orientations in different regions of the graphene are identical. In addition, we further confirmed that the coalescence of rGFs on Cu (100) results in polycrystalline graphene consisting mainly of two types of grains rotated relative to each other by 30 degrees. (Figure. 10g-i).

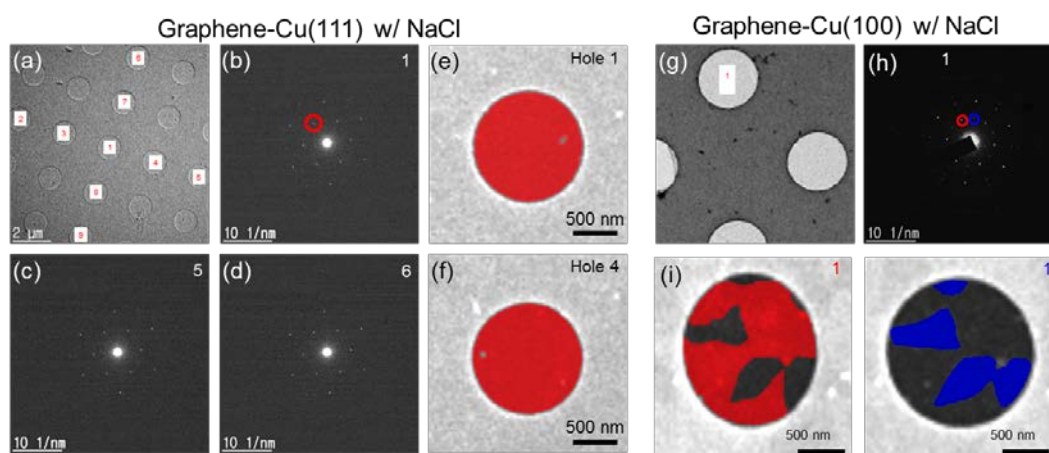


Figure 10. (a) Low magnification TEM images of graphene grown on Cu (111) with the NaCl additive. (b-d) SAED patterns collected at the holes labelled in (a). (e, f) False color DF-TEM images of the holes 1 (e) and holes 4 (f) labelled in (a), recorded with the same diffraction spot marked by red circle in (b).

(g) Low magnification TEM images of graphene grown on Cu (100) with the NaCl additive. (h) SAED pattern collected at the hole labelled 1 in (g). (i) False color DF-TEM images of the hole 1 in (g), recorded with the diffraction spots marked by red (left) and blue (right) circles in (h).

Graphene field-effect transistors (FETs) were fabricated from our single-crystal graphene sheets to explore how the crystallinity of graphene affects its electrical properties. The single-crystal graphene exhibited the large improvements in electric characteristics compared to normal graphene, with increased transconductance ($2.25 \mu\Omega^{-1}$ versus $1.05 \mu\Omega^{-1}$).

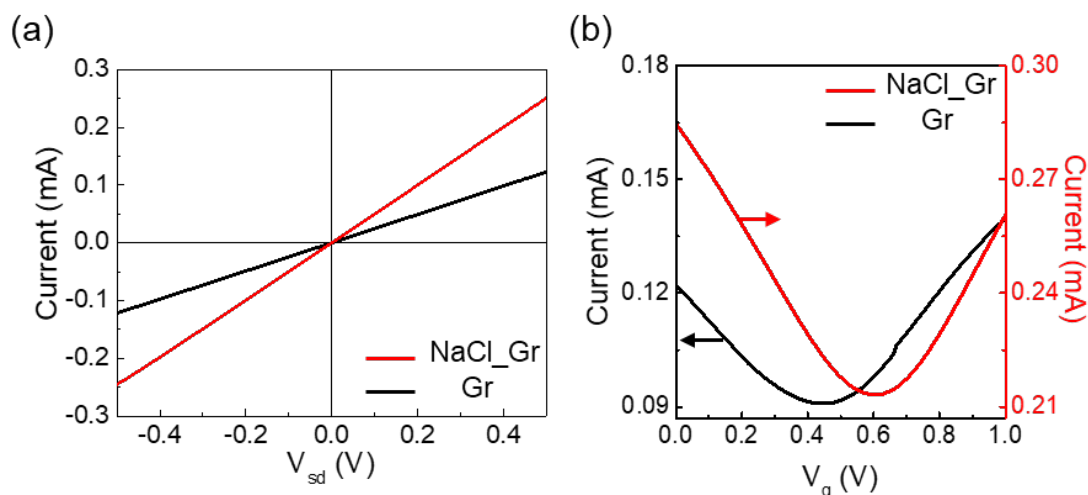


Figure 11. Current-voltage characteristics of poly-crystal (black) and single-crystal (red) graphene measured by water-gated graphene FETs. (a) I_d - V_{sd} curves without applying gate voltage. (b) I_d - V_g curves at a V_{sd} of 0.5 V.

II. Engineering edge-defects in 2D materials (zigzag vs armchair)

To obtain a mechanical understanding of the experimental observations, the first principle DFT calculation was performed on the model system. The ideal atomic configuration of the carbon lattice and the corresponding morphology of GFs were predicted through optimization of the DFT structure for the graphene-copper interface according to the surfaces of Cu (111) and Cu (100). Our DFT calculations thus show that, similar to the hGFs observed on the Cu (111) substrate grown with NaCl, the preferred stack results in hexagonal-shaped domains with zigzag edges. Stacking along the direction of Cu (100) is shown in Figure 12b, where larger unit cells were selected to match the periodicity of copper surface and graphene. Four of the six graphene hexagonal carbon atoms approximately coincide with the position of the copper atom in this case, and as a result, they coincide with the rGFs of the Cu (100) substrate to form a rectangular domain with both armchair and zigzag edges.

Based on the experimental and simulation results, it is expected that the hGFs of Cu (111) will have the same zigzag edge as the in-plane direction (Figure. 13a and b). Defect analysis was performed using a Raman spectrometer with a 532 nm excitation to confirm the effectiveness of the expectation. No noticeable D peak was observed when the Raman spectrum was obtained with a laser beam with a diameter of about $1 \mu\text{m}$ focusing on the edge of the hGFs (Figure. 13g, blue curve). This result supports our expectation that hGFs are high-quality and mainly terminate to the zigzag edge. On the other hand, if the laser beam focuses on the horizontal and vertical edges of each rGFs, one edge exhibits a distinct D peak while the other edge shows no D peak (Figure. 13g, red curve). This result is well in line with our expectation that rGFs grown in Cu (100) end with both zigzag and armchair edges (Figure. 13d,e).

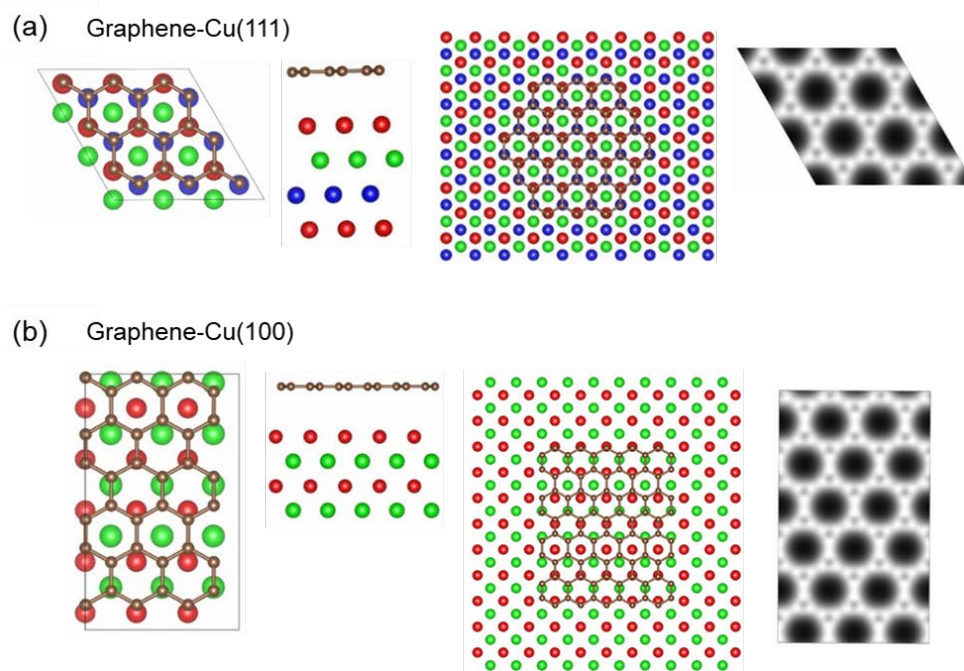


Figure 12. (a) DFT calculated graphene-Cu (111) interface and (b) graphene-Cu (100) interface. Panels from left to right indicate top and side unit cell views, the graphene domain, and scanning tunneling microscopy images, respectively. In (a) three colors are used to represent stacking for Cu (111) atom positions and in (b) two colors for Cu (100).

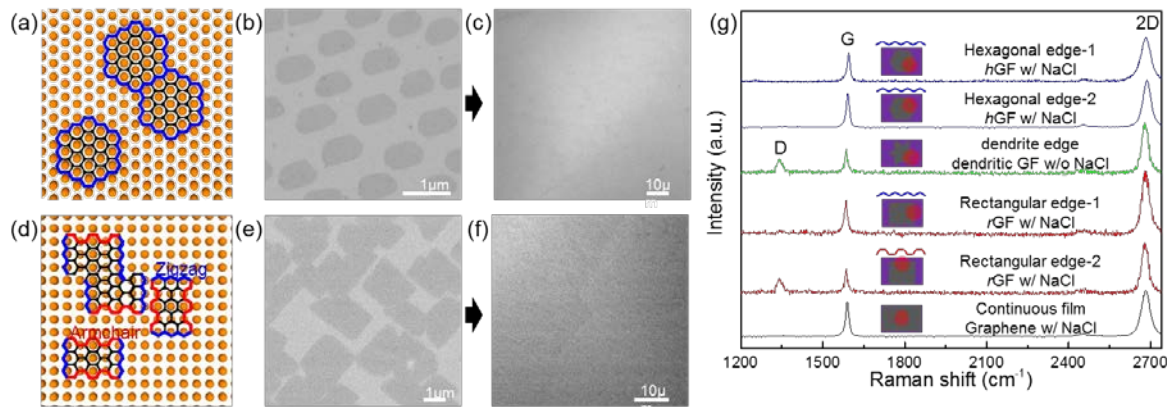


Figure 13. (a) Atomic configuration of hGFs on Cu (111) and (b, c) corresponding SEM images of GFs and continuous graphene film. (d) Atomic configuration of rGFs on Cu (100) and (e, f) SEM images of rGFs and graphene. (g) Raman spectra measured at the edges of hGFs (blue), dendrites (green), rGFs (red), and continuous graphene (black).

III. Wrinkling of Polymer film in a desired location and direction

In situ optical microscopy (OM) observations of the film with a square lattice of holes were performed immediately after removal from the solution to elucidate the wrinkle formation process (Fig. 14). We found that each midpoint between four adjacent holes first sank and adhered to the surface of the substrate (dotted regions in Fig. 14, $t = 25$ s). As time progressed,

the adhered area spread, and wrinkle formation was recognized by the appearance of straight lines connecting the holes (Fig. 14, $t \geq 40$ s). The final shape and size of the wrinkles were determined when the trapped solvent between the substrate and thin film was completely evaporated (Fig. 14, $t = 10$ m).

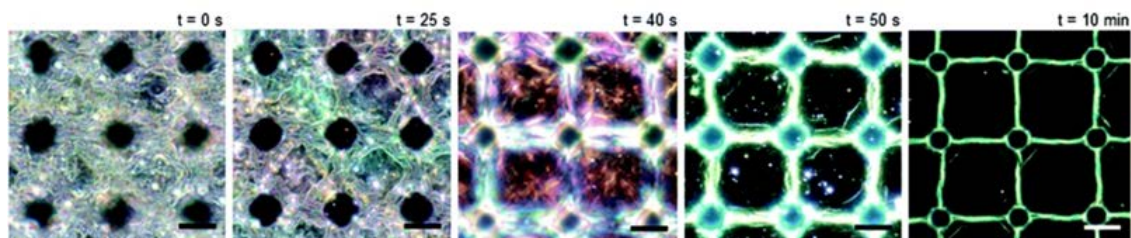


Figure 14. Hardening and wrinkling of a thin polymer film. In situ dark field microscopy images taken during wrinkling of a 25 nm thick polymer film from 0 to 10 min. Scale bars: 5 μ m.

In addition to the square lattice pattern, more discretionary patterns, such as a honeycomb lattice pattern, can be generated over a large area. Fig. 15a–c show the wrinkles that developed from a square lattice pattern with holes (a, b) and a honeycomb lattice pattern with holes (c). The straight wrinkles connecting neighboring holes show square (for the square lattice) and hexagonal shapes (for the hexagonal lattice). The dependence of the wrinkling phenomena on the hole diameter (D_h) was tested next. For instance, the number of wrinkles connecting the holes increases with D_h . Triplets and quadruplets of wrinkles formed from the square lattice patterns for D_h of 40 and 80 μ m, respectively, with an identical spacing between neighboring holes of ~ 10 μ m (Fig. 15d and e).

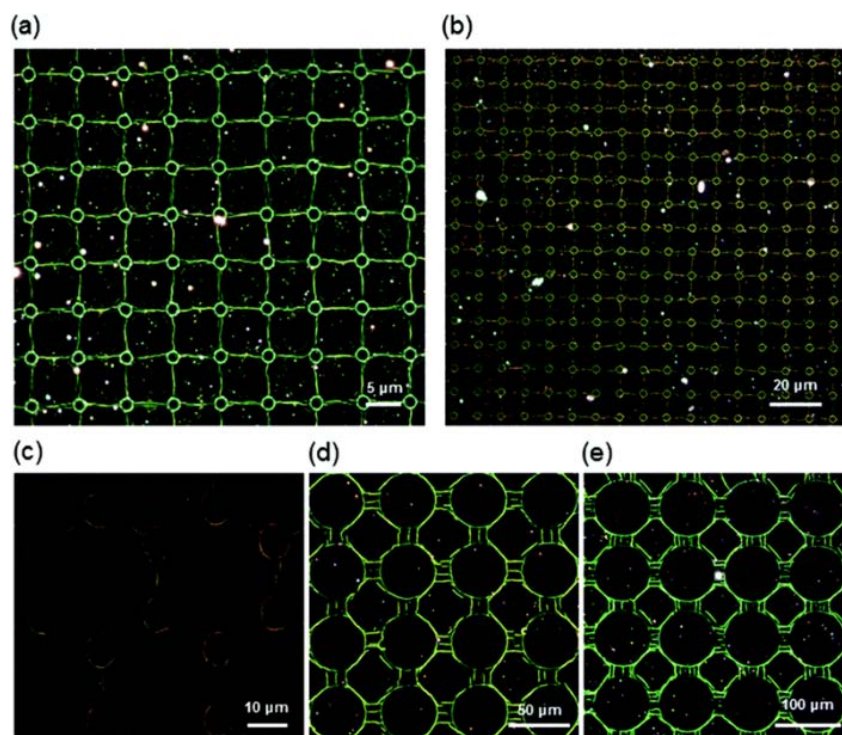


Figure 15. Dark-field OM images of diverse wrinkle structures. (a–c) Wrinkles with (a, b) square and (c) honeycomb lattice patterns. The D_h /spacing are (a, b) 3/6 μ m and (c) 10/10 μ m, respectively. (d, e) Multiplets of wrinkles from the square lattice patterns for a D_h of (d) 40 and (e) 80 μ m with an identical spacing between neighboring holes of ~ 10 μ m.

This analysis indicates that most of the fluorescent dye molecules remain inside the wrinkles and suggests the potential application of these polymer wrinkles as nano/micro-scale fluidic channels. Fig. 16a shows the geometry and defines the parameters used in this study: hole diameter (D_h), length (L), and width (W) of a unit segment marked by a white dashed square, film thickness (t), wrinkle height (H_w), wrinkle width (W_w), and elongated length (δL_w) of wrinkles compared with a flat surface. From this analysis, it was determined that δL_w is not dependent on L in the range of 20 to 90 μm (Fig. 16b, blue squares). The W_w and H_w , as well as their ratio, also exhibited a similar trend (Fig. 16b, red squares). This indicates that the elongation of the film is mostly determined by the final stage of the evaporation of the solvent trapped between the buckled film and substrate surface. In this characterization, we confirmed that the majority of the holes are entirely interconnected by the wrinkles for the L value of up to 20 μm .

Further analysis of the dependence of H_w on t revealed that H_w decreases as t increases. Minimizing U_{total} yields the following scaling law for wavelengths:

$$\lambda^2 = \left[\frac{3 \cdot E_s}{-\gamma_{p-s} + \gamma_p + \gamma_s} \right]^{\frac{3}{2}} \cdot t^{\frac{3}{2}} \cdot (-0.48t + 77)$$

The experimental values of λ^2 against $t^{3/2} \cdot (-0.48t + 77)$ are plotted in Fig. 16d, which shows quantitative agreement with the scaling relationship. This validates the scaling law derived from both the elastic deformation energy and interface energy. This also predicts that an increase in t will lead to an increase in λ and a decrease in H_w , both of which contribute to a lower aspect ratio of the wrinkles.

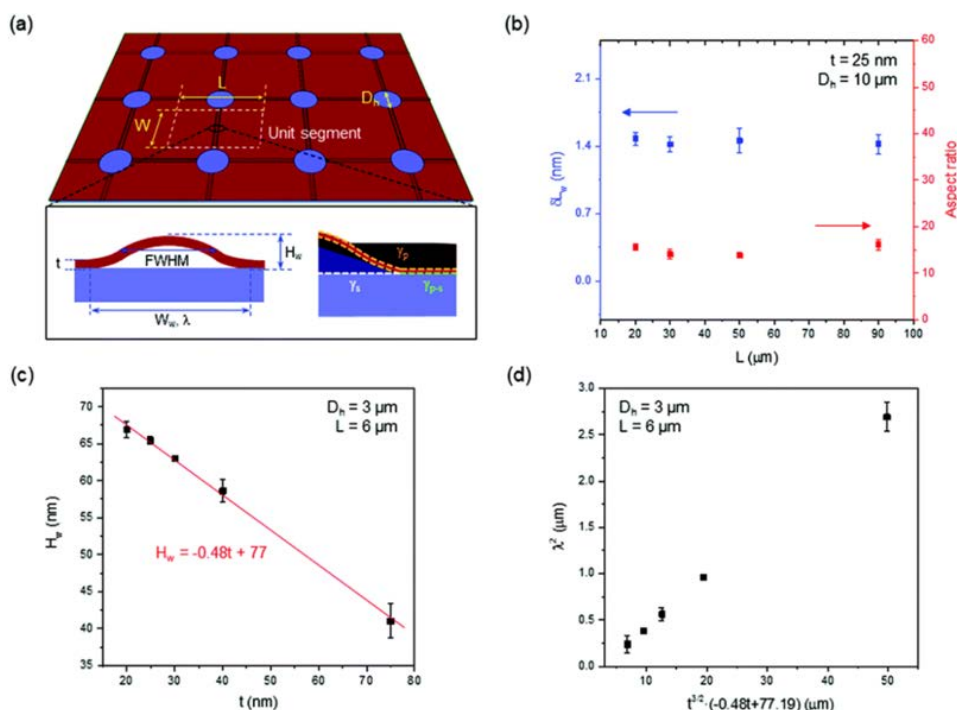


Figure 16. Analysis of the wrinkles. (a) Schematic images of the wrinkle structure with geometry and definitions of the parameters: hole diameter (D_h), center-to-center distance (D_c), length (L) and width (W) of a unit segment, film thickness (t), wrinkle height (H_w), wrinkle width (W_w), elongated length (δL_w), polymer surface (γ_p), substrate surface (γ_s), and polymer-substrate (γ_{p-s}). (b) The δL_w (blue squares) and aspect ratio (red squares) as a function of L . (c) The relationship between H_w and t ($H = -0.48t + 77$) of wrinkles. (d) Plot of λ^2 versus $t^{3/2} \cdot (-0.48t + 77)$ of wrinkles.

AFM analysis was performed for a more detailed analysis of the shape as well as the corresponding width and height of each wrinkle (Fig. 17a). The width to height ratio is larger for thinner polymer films. It was confirmed that each wrinkle continuously interconnects the neighboring holes with no substantial break. In addition to the straight wrinkles interconnecting two adjacent holes, it was also found that circular wrinkles develop along the rim of each hole.

To test the applicability of the wrinkles as nanofluidic channels, the wrinkles were filled with a solution containing a fluorescent dye. Position-dependent fluorescence intensity maps showed strong fluorescence along with the linear wrinkles and the circular rims of holes (Fig. 17b). In addition, cross-sectional profiles of the fluorescence intensity at many locations have similar shapes and full width at half maximum (FWHM) values of 0.91 ± 0.13 with less than 15% variation (Fig. 17c). Notably, the overlap of fluorescence intensity and height profile of the wrinkles shows that they have a similar intensity profile and width (Fig. 17d). This analysis indicates that most of the fluorescent dye molecules remain inside the wrinkles and suggests the potential application of these polymer wrinkles as nano/micro-scale fluidic channels.

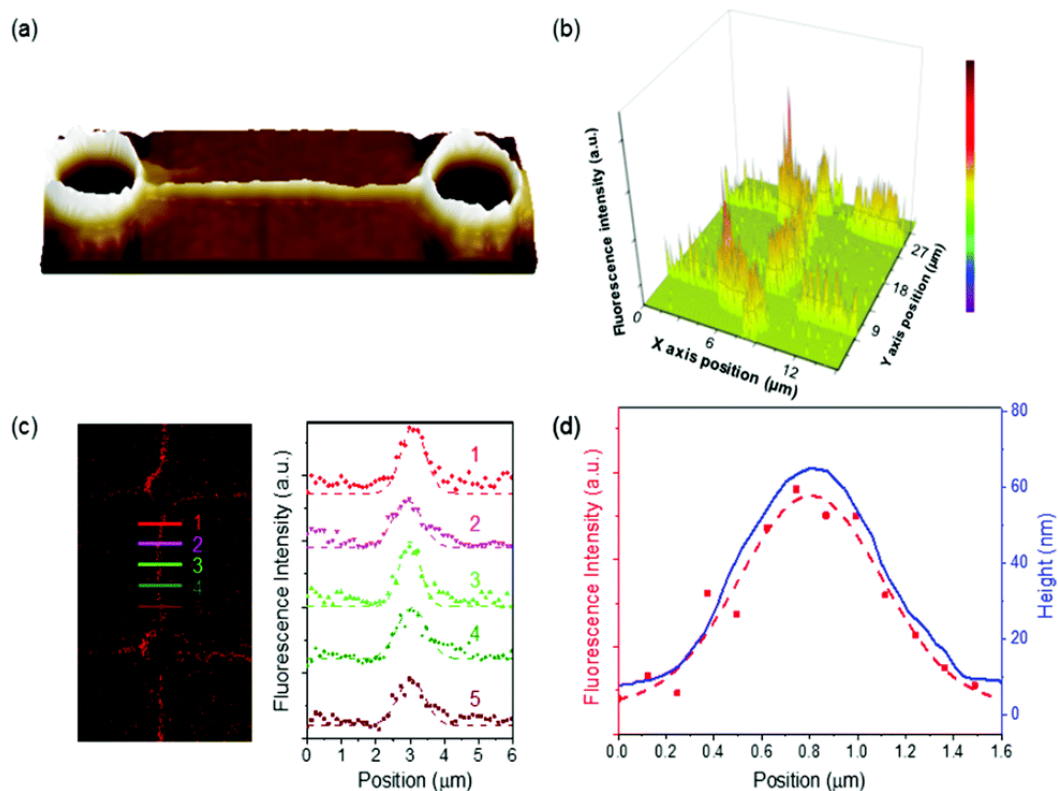


Figure 17. Utilization of polymer wrinkles as nanofluidic channels. (a) 3D AFM image of wrinkle via analysis. (b) Position-dependent fluorescence intensity map showing the distribution of the fluorescent dye along the linear and circular wrinkles. (c) Fluorescence image and the cross-sectional profiles of the fluorescence intensity at five locations. (d) Overlap of fluorescence intensity (red dots and dashed line) and height profile of the wrinkle (blue line).

IV. Wrinkling of graphene in a desired location and direction

Bright-field and dark-field optical microscopy (OM) images in Fig. 18a, b show the square lattice pattern of Gr wrinkles, with $10 \mu\text{m}$ (a) and $20 \mu\text{m}$ (b) periods, that developed over a large area. Most wrinkles were straight and interconnected the hole array only along with vertical or

horizontal directions. Scanning electron microscopy (SEM) images confirmed that the actual width of the wrinkles was about 300–500 nm (Fig. 18c). We further performed non-contact AFM analysis to determine the fine 3D features of the wrinkles between the holes (Fig. 18d).

It is important to note that our method suppressed wrinkle formation on the planar regions surrounded by wrinkles, which is analogous to ironing out wrinkles from clothes (Fig. 18e). In the case of Gr obtained by the conventional wet-transfer method, a high density of surface corrugations (wrinkles and ripples) 2 nm in height and 150 nm in width was observed over almost the entire area (Fig. 18f). This result indicates that during the gradual expansion of the adhered layer, wrinkling was not just suppressed, but intrinsic wrinkles actually unfolded.

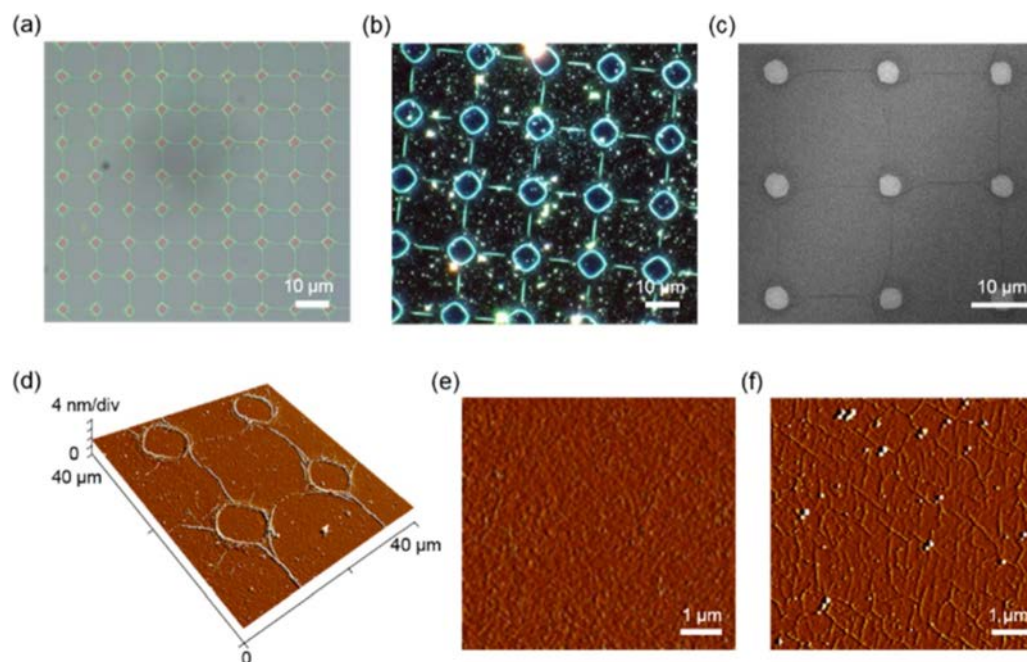


Figure 18. Structural characterization of Gr wrinkles. (a) Bright field and (b) dark field OM images, (c) SEM image, and (d) 3D AFM image of the square lattice pattern of Gr wrinkles. Hole diameters/center-to-center distances: 2 μm /10 μm (a), 8 μm /20 μm (b), 4 μm /16 μm (c) and 8 μm /20 μm (d). "(e), (f) AFM images comparing the planar region surrounded by wrinkles in (d) and that of conventional wet-transferred Gr.

To investigate structural changes before and after wrinkling, we performed Raman spectroscopy measurements. Both planar and wrinkled regions exhibited distinct 2D and G peaks at $\sim 2698\text{ cm}^{-1}$ and $\sim 1600\text{ cm}^{-1}$, respectively, with the 2D and G peak intensity ratio higher than 1 ($I_{2D}/I_G = \sim 1.4$). This result suggests that Gr was composed mostly of single layer Gr, and even after wrinkling, there was no significant tight osculation of the Gr layers. Spectra measured at different positions exhibited similar features, with an average I_{2D}/I_G ratio of 1.13 and 1.24 and an I_D/I_G ratio of 0.08 and 0.13 for planar and wrinkled regions, respectively. However, D peak intensity increased suddenly at the edges of the holes, often by more than four-fold, which is attributed to carbon disorders caused by oxygen plasma etching (Fig. 19a blue line). The similar Raman characteristics of Gr and Gr wrinkles were further supported by Raman mapping images (Fig. 19b and c). However, in our case, there is no noticeable difference in the G and 2D peak positions between the graphene regions and wrinkled regions. Considering all these Raman results, we suggest that Gr wrinkles fully recovered to a stress-free state and thereby maintained the intrinsic high structural quality of Gr, in good agreement with the stress-strain behavior results.

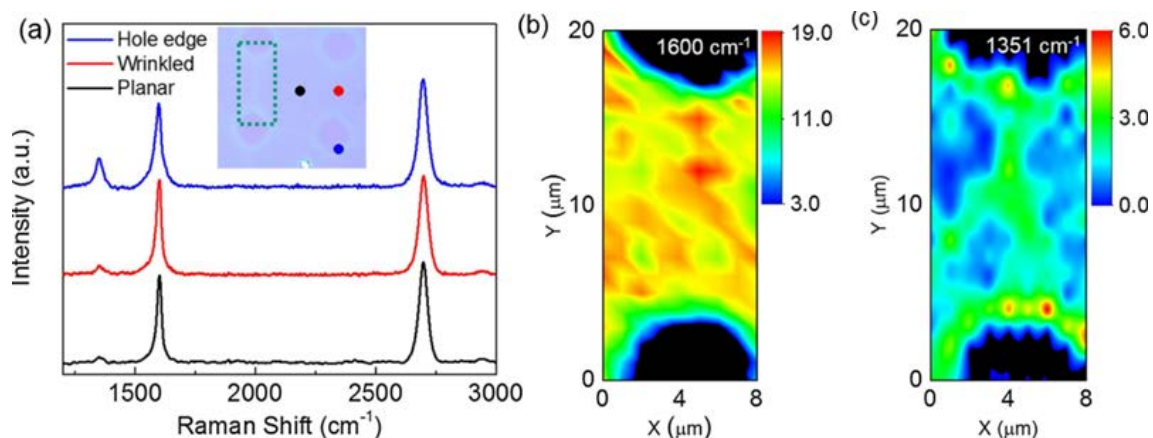


Figure 19. Raman spectroscopy analysis. (a) Raman spectra from different regions of Gr in the OM image (inset): circular edge (blue), wrinkled (red) and planar (black) regions. (b) and (c) Raman mapping images of the G peak (1600 cm^{-1}) and D peak ($\sim 1351\text{ cm}^{-1}$), collected at the dotted square area of the OM image shown in the inset of (a).

V. Selective & epitaxial growth of TMDC networks on graphene wrinkles

To confirm the uniform monolayer TMDC layer, we performed SEM, Raman spectroscopy, and photoluminescence analysis (Figure 20). From the SEM images of Figures 20a and b, it can be seen that both MoS_2 and WS_2 are uniform surfaces over the entire area. In the Raman spectra of MoS_2 and WS_2 (Figure 20c, d), we confirmed that the difference between the A_{1g} peak and the E_{12g}^1 peak of MoS_2 was 20.62 cm^{-1} , and that the A_{1g} peak intensity ratio to the E_{12g}^1 peak of WS_2 was less than 1. Also, in the PL spectra of Figures 20e and f, strong PL were confirmed for MoS_2 at 1.88 eV and WS_2 at 2.01 eV . Both Raman and PL spectra proved that MoS_2 and WS_2 films were one layer.

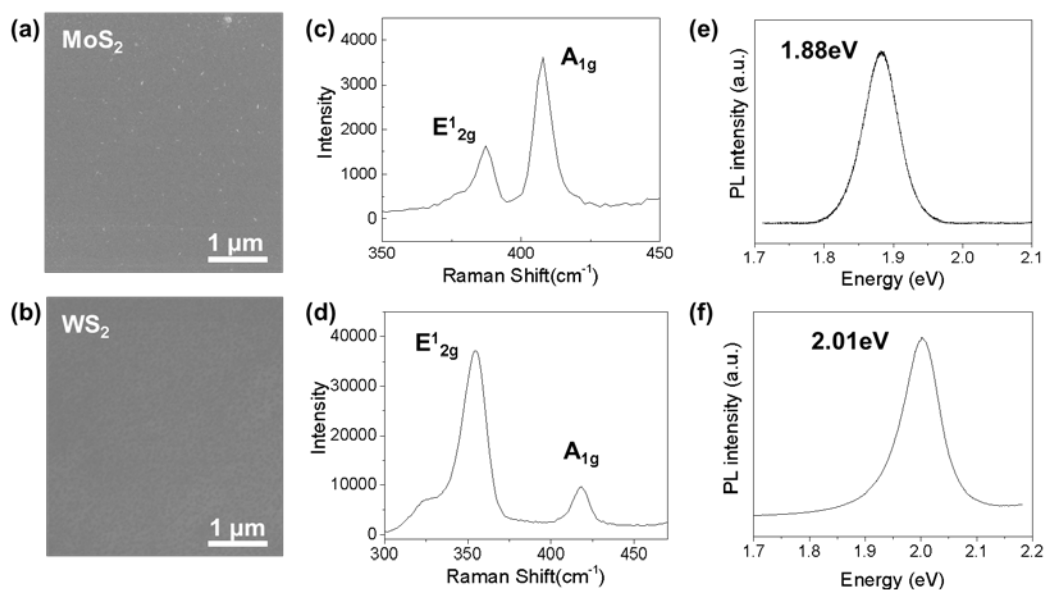


Figure 20. Characterization of MOCVD grown MoS_2 , WS_2 film. (a), (b) SEM image of MoS_2 and WS_2 film, respectively. (c), (d) Raman spectra from MoS_2 and WS_2 film. (e), (f) Photoluminescence spectra of MoS_2 and WS_2 film.

To verify the epitaxial growth of MoS₂ flakes, we analyzed SEM images of the graphene/MoS₂ heterostructure. We confirmed that MoS₂ flakes were grown aligned in two directions, including the inversion domain in both the poly-/single-graphene template (21a and b). In addition, we demonstrated that the epitaxial growth of MoS₂ occurred depending on the crystal direction of graphene from the SAED pattern and inverse FFT analysis of Figure 21g. Furthermore, we made a histogram of the growth direction of MoS₂ flakes according to the crystallinity of the graphene template (Figure 21c-f). Compared to the poly-crystal graphene template aligned in different directions according to the graphene domain, the single-crystal graphene template was aligned in only two directions in a wide range, proving the solid epitaxial growth tendency of MoS₂.

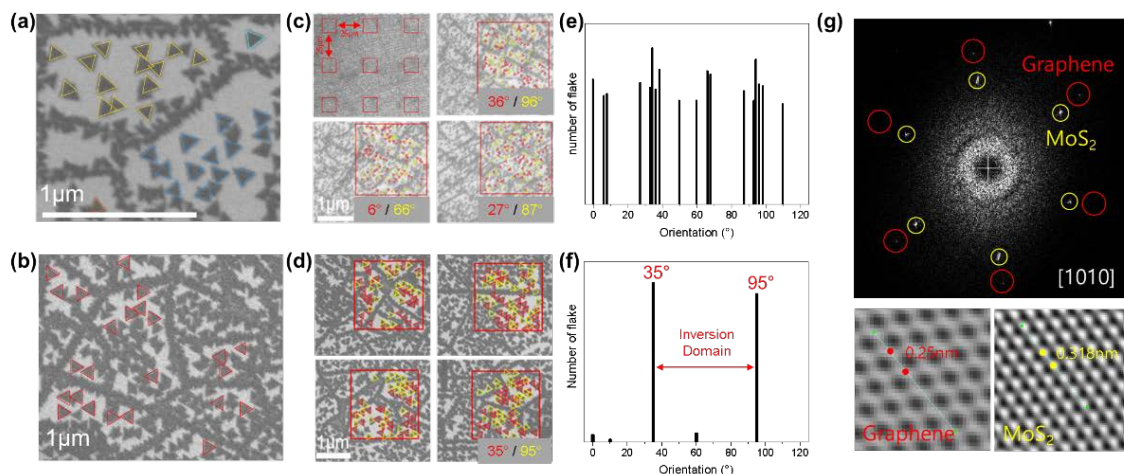


Figure 21. Characterization of graphene/MoS₂ heterostructure. SEM images of MoS₂ grown on (a) poly-crystal graphene and (b) single-crystal graphene. Each Triangles of different colors represent MoS₂ flakes grown in different orientations. SEM images of MoS₂ flakes at different positions on (c) poly-/ (d) single-crystal graphene. Red and yellow triangles indicate the inversion domain of MoS₂. (e), (f) Histograms of the number of directions in which MoS₂ flakes are aligned for each position in the SEM images of (c), (d). (g) SAED pattern of graphene/MoS₂ heterostructure (top). Inverse FFT analysis of Graphene and MoS₂, respectively (bottom)

As seen in the SEM image, it was observed that MoS₂ flakes grew along with specific defects in graphene. We demonstrated that MoS₂ was selectively grown along the wrinkles of graphene by AFM analysis of the graphene/MoS₂ heterostructure (Figure 22a and b). In addition, we performed DFT calculation and obtained the result that strained graphene adsorbs Mo and S atoms better, thereby proving that MoS₂ can be selectively grown on graphene wrinkle (Figure 22c and d).

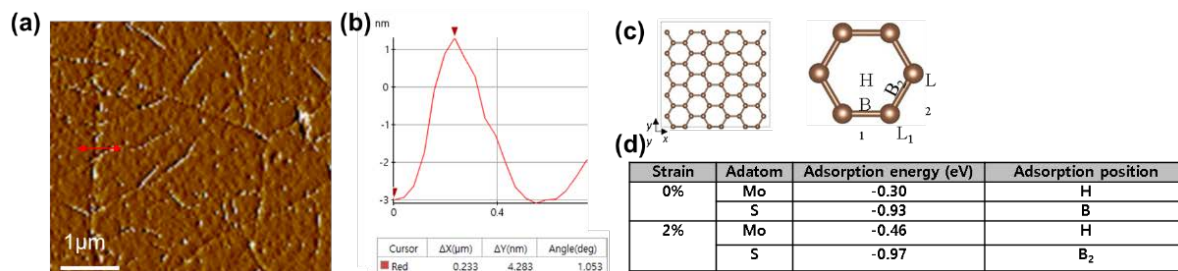


Figure 22. (a) AFM analysis of graphene/MoS₂ heterostructure. (b) Height profiling from red line of (a). (c) Graphene lattice modeling in DFT calculation. (d) Adhesion energy analysis of Mo and S atoms at strain-free graphene and 2% strained graphene.

VI. Multidimensional atomically-thin TMDC layers on diatom frustules

To characterize the Multidimensional atomically thin TMDC layers, we carried out TEM/HR-STEM characterizations (Figure 23). To characterize the few-atom-thick MoS₂ sheets directly using TEM, the specimen was prepared by carefully removing the core silica via a three-step process (Figure 23a). As shown in Fig. 23b, the annular dark field (ADF) STEM image taken at the inner hole region of the diatom cerebrum clearly shows the honeycomb lattice structures, indicating the existence of thin MoS₂ sheets. And the honeycomb pattern could be attributed to the Mo atom arrangement with a lattice spacing of 3.1 Å, which is identical to that of the monolayer MoS₂ (100) plane (Fig. 23c). It was also found that the hexagonal lattice patterns continued inside the holes, while the outside of the holes clearly exhibited different domain patterns, known as a Moiré pattern (Fig. 23d). This interference pattern is produced when a set of regular patterns is superimposed onto another set of similar (or identical) patterns with a slight offset. To investigate this feature more closely, fast Fourier transform (FFT) image analysis was carried out (Figure 23e-i). This result indicates that the MoS₂ layers on the multidimensional valves had become physically stuck to each other on the same zone-axis during the PMMA removal process

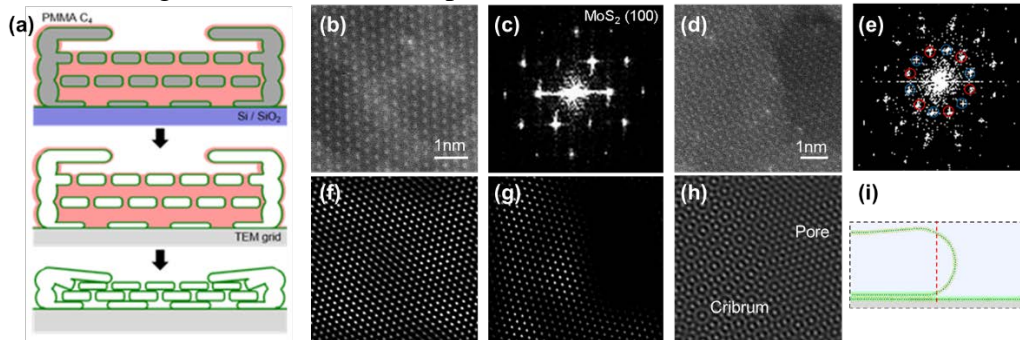


Figure 23. (a) Schematic of the processing steps (PMMA coating, silica etching, and PMMA removal with acetone vapor) for preparing TEM specimens. (b) ADF STEM image of the honeycomb lattice structures, which are observed in the inner hole region of the diatom cribrum. (c) FFT image of the Mo atom arrangement with a 3.1 Å lattice parameter, which corresponds to the monolayer MoS₂ (100) plane. (d) ADF STEM image of the boundary between the inside and outside of the holes in the diatom frustules. The inside of the holes shows the continuous hexagonal lattice patterns, while the outside exhibits a Moiré interference pattern. (e) FFT image of the entire region exhibiting two sets of hexagonal diffraction patterns (red and blue circle). iFFT patterns of each different MoS₂ monolayer, corresponding to red (f) and blue (g) circles, respectively. (h) iFFT image of both of (100) spots from the FFT patterns. (i) Schematic illustrating the sticking phenomenon of MoS₂ layers on the multidimensional valves, as determined by TEM analysis

To further analyze the crystal quality of the MoS₂ film on the diatom frustule, optical characterizations were carried out using PL and Raman spectroscopies. Fig. 24a and b show the representative PL spectra of the MoS₂ film on a SiO₂ substrate (black) and a diatom frustule (red). Both cases illustrate the strong PL emission peaks with a photon energy of approximately 1.87 eV. The Raman spectra displayed two peaks at ~383.3 cm⁻¹ and ~403.7 cm⁻¹ corresponding to the in-plane E_{2g}¹ vibration and out-of-plane A_{1g} modes of the MoS₂ crystal, respectively (Fig. 24c). The E_{2g}¹ and A_{1g} peak frequency difference of 20.4 cm⁻¹ was found for the MoS₂ films grown on the SiO₂ substrate and micro-scale diatom frustule, indicating that the MoS₂ films are mostly single layers regardless of whether they were grown on a flat or non-planar surface. These results demonstrate that single-layer MoS₂ films with direct bandgap were grown on the diatom frustules.

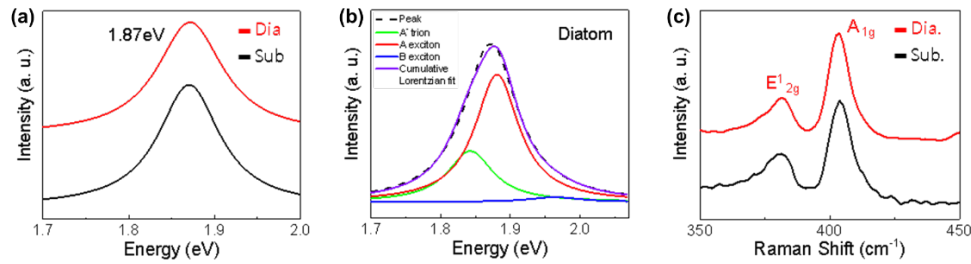


Figure 24. PL and Raman analysis of the MoS₂ diatom frustule. (a) Typical PL spectra of MoS₂ films on the Si/SiO₂ substrate (black curve) and the diatom frustule (red curve). (b) PL spectrum of the MoS₂ film on the diatom frustule fitted with three Lorentzian peaks at 1.83 eV (A⁻ trion), 1.88 eV (A exciton), and 2.03 eV (B exciton). (c) Raman spectra of MoS₂ films.

VII. MoS₂ flakes on graphene defects as a membrane for Li-ion filtering

We conducted ionic currents measurement through the MFs-on-MLFDs membrane (I_M) with two inert C electrodes to observe the Li-ion filtering properties (Figure 25a). We used the 0.1 M of LiCl aqueous solution as the electrolyte and prepared the 0.1 M of NaCl, KCl, NiCl₂, and CoCl₂ aqueous solutions for comparison. In the I_M -V curves, the MFs-on-MLFDs membrane shows superior ionic conductance in 0.1 M LiCl solution compared to the others (Figure 25b). Furthermore, it is interesting that the rectification property is observed, which indicates the Li-ion transport is more favorable with the direction along with the graphene defect to interlayer gap compared to the direction in reverse. Additionally, the chronoamperometry also shows the rectification property of the MFs-on-MLFDs membrane (Figure 25c). The saturated currents indicating the I_M showed asymmetric values depending on the ionic transport direction.

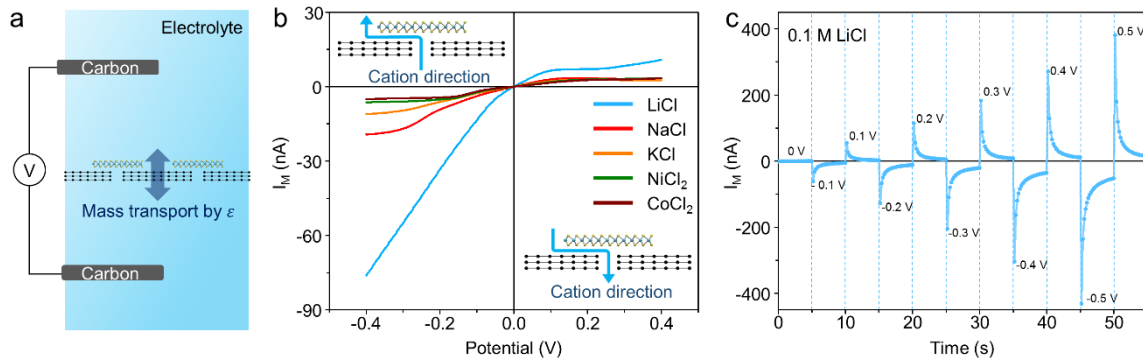


Figure 25. The scaling-up and energy-efficiency strategy using MFs-on-MLGDs membrane. (a) Schematic illustrating I_M -V measurement system. (b) I_M -V curves depending on the electrolytes. (c) Chronoamperometry.

The operation of the system is observed by the current polarization curves corresponding to the induced external bias. Interestingly, the operating performance is depending on Li-ion transport behavior by the solution level difference. When the solution level of the mixed solution is higher than that of the acidic solution, the pressure is generated toward the acidic solution, and it facilitates the Li-ion transport. In this circumstance, the system showed the normal operation with the dramatically increased current by the induced external bias (the blue curve in Figure 26a). However, when the solution level of the acid solution is higher than that

of the mixed solution, the system showed sluggish operation owing to the inhibition of Li-transport by the pressure heading to the mixed solution (the red curve in Figure 26a).

The functionality of the system was further verified by the investigation of the contamination (i.e., Na-, K-, Ni-, and Co-ions) percentages against the Li-ion. Figure 26b shows the inductively coupled plasma-mass spectrometry (ICP-MS) analysis of the collected electrolyte after each filtering round. The excellent performance of the system is confirmed by the reduced contaminations under the 3 % against the Li-ion after 3rd round of filtering.

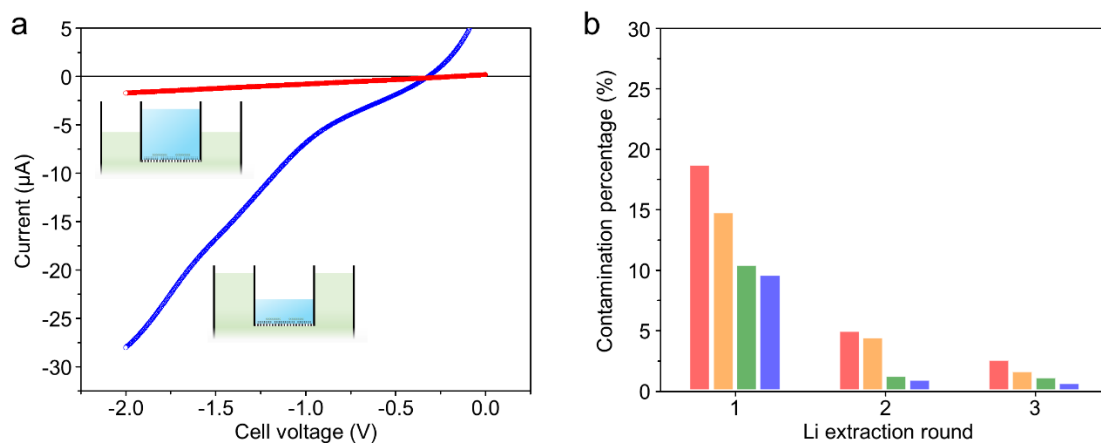


Figure 26. Operation of the system designed by the scaling-up and energy-efficiency strategies. (a) Current polarization curves depending on solution level difference. (b) ICP-MS analysis on the solutions collected after each filtering round.

Impacts

Fast growth of high quality, single-crystalline graphene using CVD

- We demonstrate a new strategy for facile chemical vapor deposition (CVD) growth of large-scale single-crystalline graphene through an unusually fast, epitaxial stitching of multiple graphene flakes (GFs).
- Investigation of early-stage growth in this process suggests that the NaCl additive enhances nucleation events and depresses dendritic growth, producing high-density GFs with crystallographically well-defined edges: (i) rectangular-shaped GFs on Cu(100) and (ii) hexagonal-shaped GFs on Cu(111).
- Single-crystal graphene can be achieved through seamless stitching of hexagonal GFs in a very short time (<90s). This study provides a guideline for achieving fast growth of high-quality, single-crystalline graphene on cheap Cu foil.

Fabricating direct nanofluidic channels via a wrinkling of thin polymer films

- We propose a rational route to create wrinkling patterns with individually controllable location and direction in thin polymer films.
- The key of our approach is to propose a more rational route to enable wrinkling in monolayer polymer films.

- We reveal that elastic energy and interface energy strongly influence out-of-plane deformation. These energies, combined with quantitative assessments of the wrinkle structures, provide insight into the scaling relationships between the height, width, and thickness of the wrinkles.
- Our analysis provides a new opportunity to finely regulate the mechanical instability in various thin films, especially including atomically thin materials, with potential applications.

Selective wrinkling of atomically thin materials

- We propose a novel wallpapering-inspired strategy to create wrinkles in a desired location and direction of 2D materials.
- The key to controlling the wrinkles is to regulate the permeation and release of solution through a regular array of holes between the substrate surface and Gr-based thin membrane (Gr/Cu in the first stage and Gr in the second stage).
- The wrinkling mechanism was further verified by in-situ optical microscopy and comparative analysis of Gr/Cu ripples and Gr wrinkles.
- Our approach is simple yet universally applicable to diverse types of thin membranes, thereby offering a robust and versatile route to engineering properties of atomically thin materials.

Multidimensional atomically-thin TMDC layers on diatom frustules

- We report on the uniform growth of atomically thin TMDC layers on diatom frustules using MOCVD.
- 3D incorporation of 2D materials can confer advanced structural, electrical, and optical functions.
- This result suggests a new capability for the 3D incorporation of 2D materials with advanced functions, thereby providing opportunities for various applications such as electronics, optoelectronics, and sensors.

MoS₂ flakes on graphene defects as a membrane for Li-ion filtering

- A successful synthesis of MoS₂ flakes on a multilayer graphene membrane (MGM) enables a scalable and energy-efficient approach for Li extraction from seawater.
- We demonstrate the multipurpose system that could filter out the Li-ions from a mixed solution and generate hydrogen gas simultaneously.
- Given that the amount of Li in seawater is about 2400 times larger than that inland, our size and surface charge-controlled 2D heterostructures membranes provide opportunities to build Li-producing plants in every area contacted with the ocean.